Near-wall behavior of RANS turbulence models and implications for wall functions

Georgi Kalitzin *, Gorazd Medic, Gianluca Iaccarino, Paul Durbin

Flow Physics and Computation Division, Department of Mechanical Engineering, Stanford University, Stanford, CA 94305-3030, USA

Abstract

The paper proposes a novel wall-function formulation applicable to any RANS turbulence model. It is based on the assumption of wall layer universality, applied to the entire model. The approach is implemented via tables for the turbulence quantities and the friction velocity u_τ. The influence of numerical errors on the wall-function solution is investigated and improvements are proposed. Numerical results are presented for a flat plate boundary layer at zero pressure gradient and for a flow with pressure gradient driven separation. The behavior of RANS turbulence models in the near wall region is also analyzed. The models considered are: Spalart–Allmaras, k–ω, k–g and v^2–f. The analysis of the v^2–f model resulted in new analytical solutions in the viscous sublayer and logarithmic layer. The analytical solutions for the Spalart–Allmaras model can be used directly as a simple wall function.
© 2004 Elsevier Inc. All rights reserved.

1. Motivation and background

The size of industrial CFD problems has grown considerably in recent years and, despite a rapid increase in computational resources, there are still many applications for which the grid resolution is insufficient for wall integration and accurate wall functions are a necessity. For example, computation of rotating stall in turbomachinery requires large scale, detailed flow-field predictions in the entire compressor [18]; assuming that a high quality grid is employed in each blade passage, the computational grid would easily exceed 50 million cells. Wall functions are also an essential ingredient for the development of Cartesian Immersed Boundary RANS methods [7]. Shortcomings of existing wall functions motivate further research in this field.

---

* Corresponding author. Tel.: +1 650 723 8476; fax: +1 650 725 3525.
  E-mail address: kalitzin@stanford.edu (G. Kalitzin).

In wall bounded flows, a large number of computational cells are generally used to resolve the boundary layers. Wall integration of turbulence models requires the first computational cell above the wall to be located within the viscous sublayer, at about $y^+ = 1$. Wall functions are meant to circumvent the excessive grid requirements. For instance, the first cell might be placed in the logarithmic layer, leading to a significant reduction in the number of cells in the boundary layer. Ideally, this is to be done without a significant loss in accuracy. In a typical wall integration grid with a normal-to-the-wall stretching of 1.15, there are about 40 cells located in the boundary layer for a momentum thickness based Reynolds number of $Re_\theta = 5000$ and only 15 cells for a corresponding wall-function grid with the first cell at $y^+ = 100$. This represents substantial savings, justifying the development and use of wall functions. The gain in computational efficiency is not only due to the smaller grid size but also to a decrease of the cell aspect ratio near the wall, which reduces computational stiffness.

The theory that lies behind wall functions is the universal character of the law-of-the-wall. This asserts that under many flow conditions the form of the solution between the wall and the outer edge of the logarithmic layer is invariant when appropriate scaling is used. From early on, with the development of the first successful RANS turbulence model [8], the universal character of the logarithmic layer has been invoked to design off-wall boundary conditions. The earliest wall functions required the first point above the wall to lie in the logarithmic layer. That is a too severe constraint, which will often be violated by the grid. If the grid point lies in the viscous sublayer, log-layer wall functions are generally very inaccurate. Wall functions that do not restrict the location of the first grid point between wall and logarithmic layer are called adaptive wall functions – or, sometimes, low y^+ wall functions. These have a long history. Several have been developed recently in [16]. The present paper addresses some of the shortcomings of the existing adaptive wall functions and aims at the development of an efficient and robust approach that is applicable to various turbulence models.

Three main issues need to be addressed in the development of adaptive wall functions. First of all, the correct physical boundary conditions need to be provided to the flow solver independently of the location of the first node above the wall. Although this sounds trivial, most approaches compromise on the conditions for the turbulence variables or on conditions in the intermediate (buffer) region. For example, in [16] a zero derivative boundary condition for the turbulent kinetic energy $dk/dy = 0$ is used throughout the boundary layer. While this is true in the viscous sublayer and in the logarithmic layer, it is far from true in the intermediate region $5 < y^+ < 30$. It is this intermediate region that presents a challenge to the adaptive approach.

The numerical accuracy is the second issue that needs to be addressed. The implication of taking the first grid point away from the wall vicinity is that the grid is relatively coarse. Fine grids are needed for wall integration because strong gradients of the flow and turbulence variables exist in the viscous layer. The truncation errors of discretized operators are significant on wall-function grids. Even if the boundary condition is proper to the location of the first cell center, numerical inaccuracy can pollute the results. This paper investigates simple corrections that alleviate these errors and improve the predictions. The separation of numerical errors from the approximation to the physics is non-trivial and requires very careful investigation.

Last but not least, the range of validity of the given wall function needs to be addressed. Criteria that restrict the maximum of the first cell center y^+ value can be derived for the given flow Reynolds number. The applicability of the proposed concept to more complex flows is assessed through the application of the adaptive wall functions to flows with pressure gradient driven separation.

The paper is organized as following. In Section 2, the near-wall behavior of four turbulence models (Spalart–Allmaras, k–ω, k–g and v^2–f) is discussed and a new wall-function formulation is proposed. The numerical implementation and the RANS flow solver used in the computations are presented in Section 3. Detailed numerical results for flow over a flat plate at zero pressure gradient and for recirculating flow with an imposed streamwise pressure gradient are presented in Section 4.

The complete equations of the turbulence models are given in Appendix A. A comparison of RANS turbulence models results with DNS data for a recirculating flow at low-Reynolds number is included in Appendix B.

2. Near-wall behavior

In this paper, we restrict our investigation to incompressible flow with constant molecular viscosity. For turbulent flow conditions, the velocity profile can be split into three distinguished regions: the viscous sublayer, the logarithmic layer and the defect layer. The location of the outer edge of the logarithmic layer depends on the Reynolds number as shown in Fig. 1(a). The extent of the logarithmic layer grows with increasing Reynolds number.

In a quasi-equilibrium boundary layer (e.g., flow over a flat plate at zero-pressure gradient), the region between the wall and the outer edge of the logarithmic layer is universal; i.e., the profiles of the flow variables collapse when scaled with the friction velocity u_τ and molecular viscosity v. This universality allows the derivation of wall functions.

Near the wall, derivatives in streamwise direction can be neglected and the flow and turbulence variables depend only on the coordinate y, which is directed normal to the wall. Essentially, this is a turbulent Couette flow approximation. To derive solutions for the viscous sublayer and logarithmic layer, the equations are recast in non-dimensional form. The velocity and various turbulence variables in plus units are:

$$U^+ = \frac{U}{u_\tau}, \quad y^+ = \frac{y u_\tau}{v}, \quad v_t^+ = \frac{v_t}{v}, \quad \tilde{v}^+ = \frac{\tilde{v}}{v}, \quad k^+ = \frac{k}{u_\tau^2}, \quad \omega^+ = \frac{\omega v}{u_\tau^2},$$

$$g^+ = \frac{g u_\tau}{\sqrt{v}}, \quad \epsilon^+ = \frac{\epsilon v}{u_\tau^4}, \quad \overline{v^2}^+ = \frac{\overline{v^2}}{u_\tau^2}, \quad f^+ = \frac{f v}{u_\tau^2}. \tag{1}$$

These variables, and the equations for the viscous sublayer and the logarithmic layer are described below for various models.
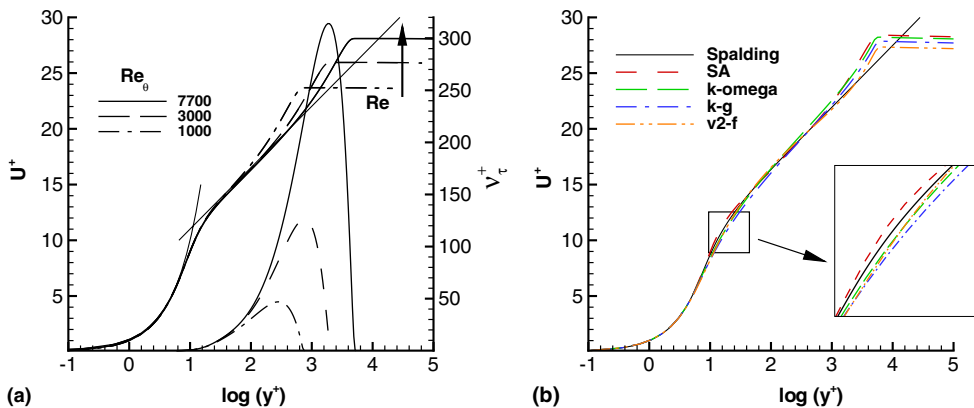

Fig. 1. Numerical solution for U^+ and v_t^+ computed using Spalart–Allmaras model with wall integration for different values of Re_θ (a) and different turbulence models compared to Spalding formula for $Re_\theta = 7700$ (b).

2.1. Reynolds-averaged Navier–Stokes equations

As explained above, for the flow over a flat plate at zero-pressure gradient the RANS equations simplify in the region between the wall and the outer edge of the logarithmic layer to

$$\frac{\mathrm{d}}{\mathrm{d}y}\left((\mu + \mu_\mathrm{t})\frac{\mathrm{d}U}{\mathrm{d}y}\right) = 0. \tag{2}$$

Integration along the wall normal coordinate y yields

$$(\mu + \mu_\mathrm{t})\frac{\mathrm{d}U}{\mathrm{d}y} = \rho u_\tau^2. \tag{3}$$

This equation states that the sum of the viscous and turbulent shear stress is constant and equal to the wall shear stress $\tau_\mathrm{w} = \mu(\partial u/\partial y)_\mathrm{w} = \rho u_\tau^2$. Introducing the non-dimensionalization (1), Eq. (3) becomes

$$(1 + v_\mathrm{t}^+)\frac{\mathrm{d}U^+}{\mathrm{d}y^+} = 1. \tag{4}$$

The linear law, $U^+ = y^+$, follows for the viscous sublayer where $v_\mathrm{t}^+ \ll 1$. In the logarithmic layer, v_t^+ is large and Eq. (4) is usually approximated with

$$v_\mathrm{t}^+\frac{\mathrm{d}U^+}{\mathrm{d}y^+} = 1. \tag{5}$$

Using Prandtl's assumption for the turbulent viscosity [12],

$$v_\mathrm{t}^+ = \kappa y^+, \tag{6}$$

the logarithmic law $U^+ = (1/\kappa)\log(y^+) + B_{\log}$ follows with the experimentally fitted constants $\kappa = 0.41$ and $B_{\log} = 5.0$.

Suppose v_t^+ were known. Then (4) could be integrated to find the universal function $U^+(y^+)$. An early approach was to assume a form for that function, such as Spalding's profile [15]. However, it is more consistent to develop the function that is appropriate to each model by solving the wall layer equations numerically. Now, knowing the universal function, the friction velocity can be solved from the computed velocity at the first grid point. Say that is U_1, evaluated at y_1. If this lies in the wall layer, then

$$Re_y \equiv y_1 U_1/v = y_1^+ U^+(y_1^+) = F(y_1^+), \tag{7}$$

Re_y is the Reynolds number obtained from the first cell. The right is a universal function. Inverting this function gives

$$y_1 u_\tau/v = F^{-1}(Re_y).$$

Hence, u_τ can be found. Given $F(y_1^+)$, the inversion can be done iteratively by Newton's method. However, this can be done once and for all, and the inverse function stored in a table [5]. That is the method used in our computations. In a finite volume formulation, the friction velocity is used in the momentum balance. Hence, it serves as a boundary condition for computing U_1. In a finite difference formulation, (4) provides a velocity gradient boundary condition.

The eddy-viscosity is explicitly related to the velocity profile. In the entire region between the wall an the outer edge of the logarithmic boundary layer the eddy-viscosity is related to the velocity gradient according to Eq. (4):

$$v_\mathrm{t}^+ = \frac{\mathrm{d}y^+}{\mathrm{d}U^+} - 1. \tag{8}$$

In some wall-function formulations, the velocity profile and eddy-viscosity do not obey this relation. The result is grid dependence. One might use (8) to obtain a boundary condition on one turbulence variable, thereby ensuring consistency between the eddy-viscosity and the velocity gradient: for instance, in the k–ω model, the k condition can be obtained from (8), given a condition on ω. In the present paper, consistency comes from solving the model equation in the wall layer. Formally, the wall function should match smoothly to the outer, computational region. Consistent matching would produce a grid independent formulation – although the issue of numerical accuracy must be addressed and the assumption of quasi-equilibrium is a caveat.

For the turbulence equations, analytical solutions can often be derived for the viscous sublayer and for logarithmic layer. However, the intermediate region is problematic. This can be addressed by generating a look-up table for each non-dimensionalized turbulence variable from a well-resolved numerical solution. This table can take the form of spline coefficients. The analytical solutions in the viscous sublayer and the logarithmic layer for the Spalart–Allmaras, k–ω, k–g and v^2–f models are discussed in the next section.

2.2. Spalart–Allmaras model

Near the wall, Eq. (A.3) can be written as

$$c_{b1}(1 - f_{t2})\tilde{S}^+\tilde{v}^+ + \left(\frac{c_{b1}}{\kappa^2}f_{t2} - c_{w1}f_w\right)\left(\frac{\tilde{v}^+}{y^+}\right)^2 + \frac{c_{b2}}{c_{b3}}\left(\frac{d\tilde{v}^+}{dy^+}\right)^2 + \frac{1}{c_{b3}}\frac{d}{dy^+}\left((1 + \tilde{v}^+)\frac{d\tilde{v}^+}{dy^+}\right) = 0, \tag{9}$$

where $\tilde{v}^+ \equiv \chi$.

In the viscous sublayer, the functions $f_{v1} \to 0$, $f_{v2} \to 1 - \tilde{v}^+$ and $f_w \to 1$. The strain is $S^+ = dU^+/dy^+ = 1$ and the dominant term in the modified strain is $\tilde{S}^+ = \tilde{v}^+/(\kappa^2(y^+)^2)$. Eq. (9) can be simplified to

$$(1 + c_{b2})\left(\left(\frac{d\tilde{v}^+}{dy^+}\right)^2 - \left(\frac{\tilde{v}^+}{y^+}\right)^2\right) + (1 + \tilde{v}^+)\frac{d^2\tilde{v}^+}{(dy^+)^2} = 0. \tag{10}$$

The function $\tilde{v}^+ = \kappa y^+$ satisfies Eq. (10), i.e. $\tilde{v}^+$ varies linearly in the viscous sublayer. The eddy-viscosity $v_t^+ = \tilde{v}^+ f_{v1}$ varies as $(y^+)^4$.

It can easily be shown that in the log-layer $\tilde{v}^+ = v_t^+ = \kappa y^+$. Indeed, one of the elements of this model is to formulate the $\tilde{v}$-equation such that $\tilde{v}$ is approximately linear from the log-layer to the wall.

Near-wall behavior of eddy-viscosity v_t^+ and $\tilde{v}^+$ is presented in Fig. 2. $\tilde{v}^+$ is indeed approximately linear in the entire wall layer and the slope is approximately equal to κ.
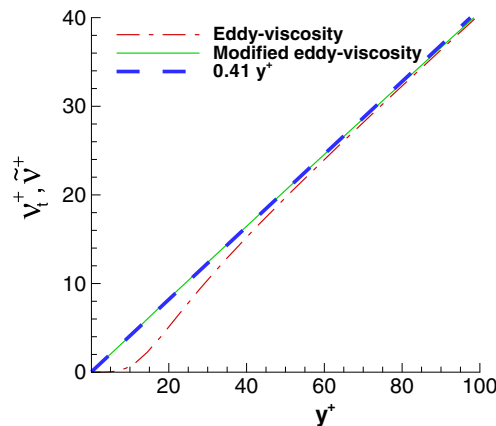
Fig. 2. Eddy-viscosity v_t^+ and modified eddy-viscosity $\tilde{v}^+$ for Spalart–Allmaras model.

Since Spalart–Allmaras is a one-equation model, a wall function can be derived without any prior knowledge about the behavior of $\tilde{v}^+$ in the near-wall region. The eddy-viscosity is computed from Eq. (8) and $\tilde{v}^+$ is computed from the eddy-viscosity definition: $\tilde{v}^+ = v_t^+/f_{v1}$. This must be solved iteratively, but, as mentioned previously, that can be done once, and the inverse function stored tabularly.

Alternatively, the linear behavior of $\tilde{v}^+$ between the wall and outer edge of the logarithmic layer can be used to define an adaptive wall function:

$$\tilde{v}^+ = \kappa y^+, \quad v_t^+ = \tilde{v}^+ f_{v1}, \quad f_{v1} = \frac{(\tilde{v}^+)^3}{(\tilde{v}^+)^3 + c_{v1}^3}. \tag{11}$$

2.3. k–ω model

In the viscous sublayer, the equations of the standard k–ω model (A.13) and (A.15) reduce to

$$-C_\mu \omega^+ k^+ + \frac{d^2 k^+}{(dy^+)^2} = 0, \tag{12}$$

$$-\beta_1 (\omega^+)^2 + \frac{d^2 \omega^+}{(dy^+)^2} = 0. \tag{13}$$

Eq. (13) has the singular solution

$$\omega^+ = \frac{6}{\beta_1 (y^+)^2}. \tag{14}$$

Non-singular solutions also exist, but this is considered the appropriate solution for smooth walls [17].

Wilcox has shown in [17] that the numerical discretization of such a function causes serious numerical errors in the viscous sublayer. He suggested to enforce the analytical solution (14) in all points in the computational grid for which $y^+ < 2.5$.

Using expression (14), Eq. (12) can be solved for turbulent kinetic energy in the viscous sublayer

$$k^+ = C_k (y^+)^{3.23}. \tag{15}$$

This equation satisfies the boundary conditions $k^+(0) = 0$ and $dk^+/dy^+(0) = 0$. The eddy-viscosity, $v_t^+ = k^+/\omega^+$, varies as $(y^+)^{5.23}$ in the viscous sublayer.

In the logarithmic layer, the k–Eq. (A.13) is:

$$\frac{d}{dy^+}\left(\sigma_k v_t^+ \frac{dk^+}{dy^+}\right) + v_t^+ \left|\frac{dU^+}{dy^+}\right|^2 - C_\mu \omega^+ k^+ = 0. \tag{16}$$

The diffusion term is usually assumed to be small compared to the other two terms. Setting it to zero implies that the diffusive flux is constant

$$\sigma_k v_t^+ \frac{dk^+}{dy^+} = C_k. \tag{17}$$

The eddy-viscosity in the logarithmic layer is approximately $v_t^+ = \kappa y^+$ and Eq. (17) can be integrated as

$$k^+ = \frac{C_k}{\sigma_k \kappa} \log(y^+) + B_k. \tag{18}$$

The balance of production and dissipation in Eq. (16) provides an expression for the specific dissipation rate. Using $k^+ = v_t^+ \omega^+$ gives $\omega^+ = |dU^+/dy^+|/\sqrt{C_\mu}$ or

$$\omega^+ = \frac{1}{\kappa\sqrt{C_\mu}y^+}, \tag{19}$$

which uses the relation (5) between velocity gradient and eddy-viscosity. k^+ follows:

$$k^+ = \frac{1}{\sqrt{C_\mu}}. \tag{20}$$

Thus, the turbulent kinetic energy is constant in the logarithmic layer and the constant C_k in Eq. (17) is zero for this model.

In the intermediate region, ω^+ is usually approximated with some form of interpolation between the viscous sublayer value ω_{vis}^+ (Eq. (14)) and the log-layer value ω_{log}^+ (Eq. (19)). In [16], it is suggested:

$$\omega^+(y^+) = \sqrt{[\omega_{\mathrm{vis}}^+(y^+)]^2 + [\omega_{\mathrm{log}}^+(y^+)]^2}. \tag{21}$$

An alternative to Eq. (21) is to solve the model equations and develop a tabulated curve fit. A comparison between a look-up table value for ω^+ and Eq. (21) reveals a discrepancy for the intermediate region. Using a look-up table obtained from the numerical solution is superior.

There are no satisfactory interpolation formula for k^+ given in the literature [19–21], and usually the condition $dk^+/dy^+ = 0$ is applied [16]. However, this is only correct at the wall and in the logarithmic layer. It is incorrect in the intermediate region. A boundary condition on k^+ that is consistent with ω^+ and the velocity profile is

$$k^+ = v_t^+ \omega^+ = \left(\frac{dy^+}{dU^+} - 1\right)\omega^+. \tag{22}$$

This could be used with Spalding's formula for dy^+/dU^+ or with the velocity profile tabulated from a computational solution.

2.4. k–g model

The k–g model [6] is derived from the k–ω model by substituting ω with g:

$$g^+ = \sqrt{\frac{1}{C_\mu \omega^+}}. \tag{23}$$

In the viscous sublayer, ω^+ is given by Eq. (14) and therefore g^+ behaves as

$$g^+ = \sqrt{\frac{\beta_1}{6C_\mu}y^+}. \tag{24}$$

In the logarithmic layer, g^+ is

$$g^+ = \sqrt{\frac{\kappa y^+}{\sqrt{C_\mu}}}. \tag{25}$$

2.5. v^2–f model

The analysis in this section is given for the general version of the v^2–f model [9] and is valid for $N = 1$ or $N = 6$. The numerical simulation was carried out for $N = 6$ and, therefore, any coefficients that result from the numerical solution are valid only for that version.

In the viscous sublayer, the v^2–f-equations reduce to:

$$\left.\begin{aligned}
&-\varepsilon^+ + \frac{\mathrm{d}^2 k^+}{(\mathrm{d}y^+)^2} = 0, \\
&-\frac{C_{\varepsilon2}}{6}\left(\varepsilon^+\right)^{1.5} + \frac{\mathrm{d}^2\varepsilon^+}{(\mathrm{d}y^+)^2} = 0, \\
&-N\frac{\varepsilon^+(\overline{v^2})^+}{k^+} + k^+ f^+ + \frac{\mathrm{d}^2(\overline{v^2})^+}{(\mathrm{d}y^+)^2} = 0, \\
&\frac{2}{3}(C_{f1}-1) - (N-C_{f1})\frac{(\overline{v^2})^+}{k^+} - \frac{6}{(\varepsilon^+)^{0.5}}f^+ + \frac{C_\eta^2 C_L^2 6}{\varepsilon^+}\frac{\mathrm{d}^2 f^+}{(\mathrm{d}y^+)^2} = 0,
\end{aligned}\right\} \tag{26}$$

in which the Kolmogoroff limit has been used for the time scale T and length scale L.

The ε^+–Eq. (26) is decoupled from the rest of the equations. An analytical solution of this equation is

$$\varepsilon^+ = \frac{14{,}400}{C_{\epsilon2}^2}\frac{1}{\left(y^+ + C\right)^4}. \tag{27}$$

Using the solution for ε^+, the k^+–Eq. (26) can also be integrated analytically (with the boundary conditions: $k^+(0) = 0$ and $\mathrm{d}k^+/\mathrm{d}y^+(0) = 0$):

$$k^+ = \frac{2400}{C_{\epsilon2}^2}\left[\frac{1}{\left(y^+ + C\right)^2} + \frac{2y^+}{C^3} - \frac{1}{C^2}\right]. \tag{28}$$

A single integration constant has been allowed in Eqs. (27) and (28). To obtain a unique solution, an additional condition is required. In [3], a locally quadratic behavior is imposed on k^+ by assuming $k^+ = C_k(y^+)^2$. Introducing this in Eq. (26) provides a condition for ε^+:

$$\varepsilon^+ = 2\frac{k^+}{(y^+)^2}, \tag{29}$$

which can be used as a boundary condition by imposing $\varepsilon_w^+ \approx \varepsilon_1^+ = 2k_1^+/(y_1^+)^2$. The constant C can now be computed from a numerical solution, which gives approximately $C \approx 11.0$.

The f^+ equation can be solved if the term $(N-C_{f1})((\overline{v^2})^+/k^+)$ in (26) is neglected:

$$f^+ = C_1(y + C)^{\frac{1}{2}+\sqrt{D}} + C_2(y + C)^{\frac{1}{2}-\sqrt{D}} - \frac{0.1188}{(y + C)^2}, \tag{30}$$

where $D = \frac{1}{4} + \frac{120}{C_\eta^2 C_L^2 C_{\epsilon2}}$.

In [3], a boundary condition for f^+ is derived by assuming that $(\overline{v^2})^+$ behaves locally as $(\overline{v^2})^+ = C_{v2}(y^+)^4$ and introducing that in Eq. (26):

$$f^+ = \frac{-4(6 - N)(\overline{v^2})^+}{\varepsilon^+(y^+)^4}. \tag{31}$$

Using this boundary condition, the coefficients C_1 and C_2 in (30) can be adjusted to fit the numerical solution for f^+ ($C_1 = 0.000505$ and $C_2 = -0.004950$). The solution for f^+ fits the numerical solution perfectly, as shown in Fig. 3. This might mean that the term $(N-C_{f1})(\overline{v^2})^+/k^+$ in the f^+-equation has limited impact in the viscous sublayer.

The eddy-viscosity, $v_t^+ = C_\mu(\overline{v^2})^+ T^+ = 6C_\mu(\overline{v^2})^+/\sqrt{\varepsilon^+}$, varies locally as $(y^+)^4$. A comparison of eddy-viscosity profiles in the near-wall region computed with various turbulence models is presented in Fig. 4.

In the logarithmic layer, the k and $\overline{v^2}$–Eqs. (A.24) and (A.26), respectively, are:

$$\frac{\mathrm{d}}{\mathrm{d}y^+}\left(v_t^+\frac{\mathrm{d}k^+}{\mathrm{d}y^+}\right) + v_t^+\left|\frac{\mathrm{d}U^+}{\mathrm{d}y^+}\right|^2 - \varepsilon^+ = 0, \tag{32}$$
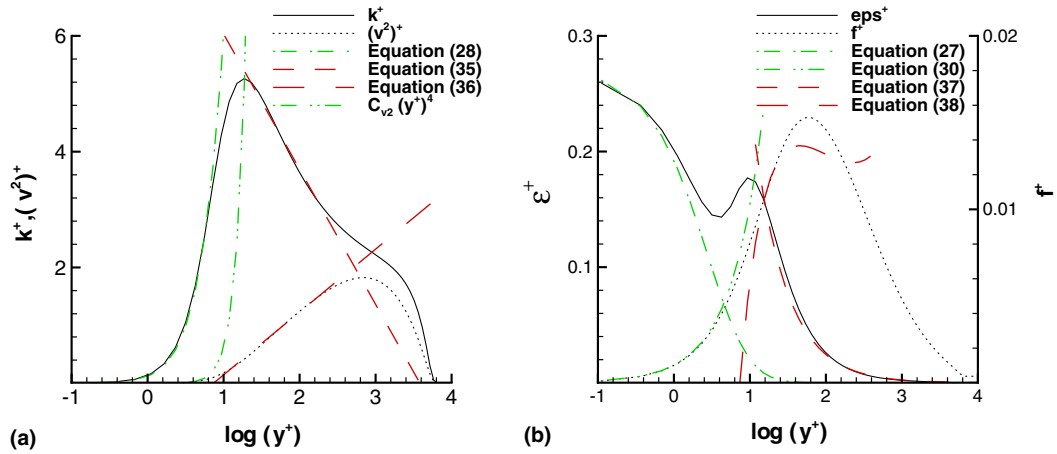
Fig. 3. Numerical solution for k^+, $(\overline{v^2})^+$, ε^+ and f^+ computed using wall integration vs. theoretical solution.
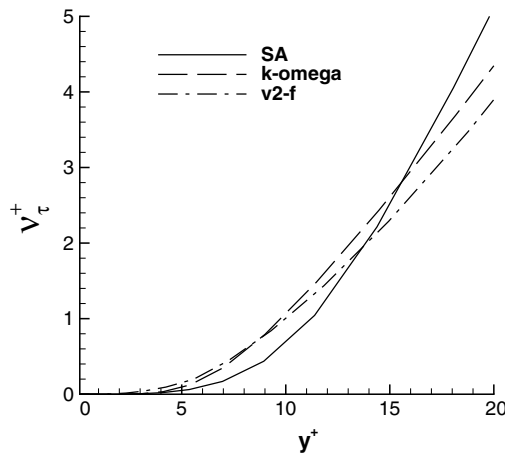

Fig. 4. Eddy-viscosity in near-wall region.

$$\frac{\mathrm{d}}{\mathrm{d}y^+}\left(v_\mathrm{t}^+\frac{\mathrm{d}(\overline{v^2})^+}{\mathrm{d}y^+}\right) + k^+f^+ - N\frac{(\overline{v^2})^+}{k^+}\varepsilon^+ = 0. \tag{33}$$

As before, diffusion is assumed to be small compared to the other two terms. The assumption that the diffusion term in Eq. (32) is small means that diffusive flux is constant:

$$\kappa y^+\frac{\mathrm{d}k^+}{\mathrm{d}y^+} = C_k. \tag{34}$$

Integrating, Eq. (34) yields

$$k^+ = \frac{C_k}{\kappa}\log(y^+) + B_k. \tag{35}$$

In the same way,

$$(\overline{v^2})^+ = \frac{C_{v2}}{\kappa} \log(y^+) + B_{v2}. \tag{36}$$

From (32), using $\mathrm{d}U^+/\mathrm{d}y^+ = 1/(v_t^+)$ we have

$$\varepsilon^+ = \frac{1}{v_t^+} = \frac{1}{\kappa y^+}. \tag{37}$$

Similarly, from (33) we have

$$f^+ = N \frac{(\overline{v^2})^+}{(k^+)^2} \varepsilon^+. \tag{38}$$

A fit to the numerical solution of v^2–f model in the log-layer gives the following values for the constants (see Fig. 3):

$$C_k = -0.416, \quad B_k = 8.366, \quad C_{v2} = 0.193, \quad B_{v2} = -0.940. \tag{39}$$

The logarithmic behavior of the turbulent kinetic energy in the logarithmic layer is supported by direct numerical simulation (DNS) [14] and experimental data at higher Reynolds numbers [2]. The DNS data were fit by [14]

$$C_k = -0.36, \quad B_k = 8.15. \tag{40}$$

The DNS (40) and v^2–f (39) values are similar. Note that the DNS was carried out at $Re_\theta = 1410$ and the model results were obtained for $Re_\theta = 7700$.

3. Numerical implementation

The adaptive wall functions described above are implemented in a three-dimensional, Cartesian, incompressible RANS flow solver [7]. It is based on a standard, cell centered SIMPLE algorithm. The momentum equation for each velocity component, Poisson equation for the pressure and transport equations for the turbulence variables are solved sequentially with a fully implicit numerical scheme. A blending of second-order central differences with first-order upwind is employed for the convection terms and second-order central differences are used for the discretization of the diffusion terms. Halo cells are used to impose boundary condition.

There are many ways to implement wall functions into a Navier–Stokes code. However, the main ingredients are as follows. The u-velocity component requires a condition that ensures the correct shear stress at the wall (Eq. (3)). Since the diffusion term is treated implicitly here, the correct wall flux is included as an explicit correction on the right-hand side. To compute the correction, u_τ is needed. As explained in Section 2.1 using the values y_1 and U_1 from the first cell center a local Reynolds number Re_y is computed. A value of u_τ is obtained from the corresponding look-up table.

The look-up tables were created from an accurate numerical wall integration solution of a flow over a flat plate at zero-pressure gradient. At a sufficiently high Reynolds number ($Re_\theta > 5000$) profiles of non-dimensional variables were approximated using cubic splines. For variables with large variations in the boundary layer the curve fit is done for their logarithm (e.g. $\log \omega^+$ is fitted in place of ω^+). This reduces the interpolation error.

An off-wall boundary condition is adopted for the turbulence variables by enforcing the first cell-center values. These values can be obtained from the near-wall behavior of turbulence models. If the first cell cen-

ter y_1^+ lies in the viscous sublayer or in the logarithmic layer, the analytical expressions given in the previous sections can be used directly. For the intermediate region, interpolation formula are needed. Alternatively, a look-up table for each variable can be used in the entire near-wall region. This approach has been adopted for the numerical simulations in this paper.

4. Numerical results

Wall functions are designed to be used with coarse near-wall grids. The solution of the discrete RANS equations is associated with a numerical error that increases with decreasing grid resolution. The difficulty in testing wall-function implementations is to distinguish between this numerical error and inaccuracies that may result from the physical model. What we will call a δ-grid eliminates the numerical error and provides a test for the correctness of the applied boundary conditions. In the δ-grid, a wall integration grid is shifted by a distance δ into the flow to provide the desired y^+ location of the first cell as shown in Fig. 5. The wall functions provide the desired boundary conditions. At the same time, the grid resolution and the associated numerical error is of the same order as for the wall integration. Note that this grid is only used to test the physical boundary conditions. Standard grids are subsequently used to test the adaptive wall functions.

4.1. Flow over flat plate

Flow over a flat plate was solved to the downstream location defined by momentum thickness based Reynolds number of $Re_\theta = 7700$. All turbulence models have been solved on δ-grids with first cell center at $y^+ = 0.11, 1.1, 2.5, 5, 11, 25, 111$. After considering the δ-grid, solutions will be given on standard coarsened grids with the same first cell center y^+ values.

When δ-grids are used with the correct boundary conditions, the computations collapse onto the wall integration profile. This is true for all the models considered, as shown in Fig. 6. Since the results for all the grids are practically coinciding, the colors of the curves are chosen to alternate between grey and black to visualize the first grid point for each grid.

The results obtained on "classic" coarse grids are presented in Fig. 7. The spread in the results is the consequence of numerical errors. This is inferred from the fact that solutions on the δ-grids collapse on the wall integration result.
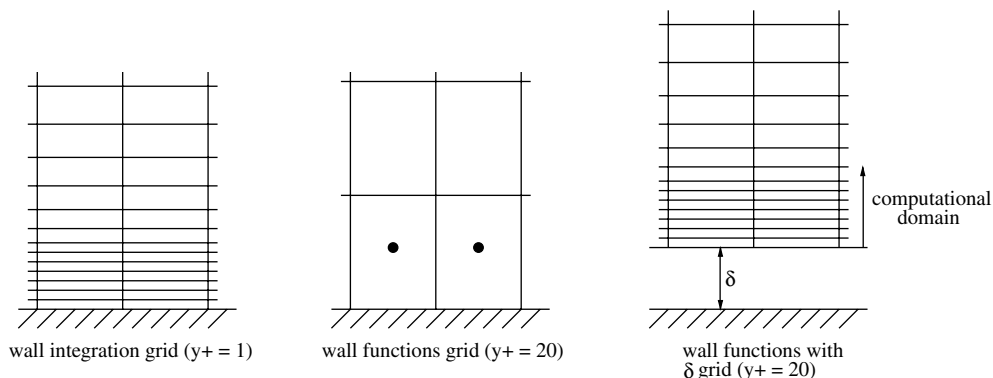

wall integration grid (y+ = 1)   wall functions grid (y+ = 20)   wall functions with
                                                                               δ grid (y+ = 20)

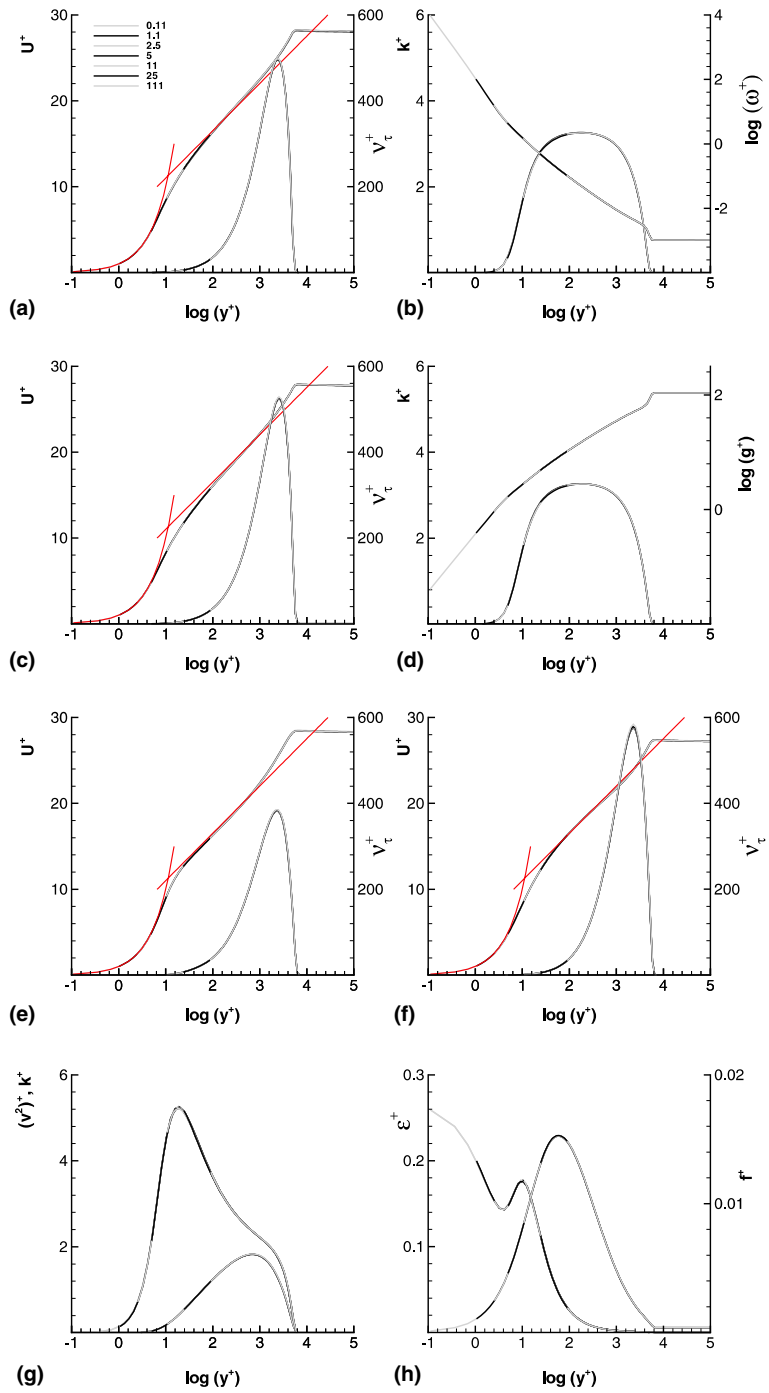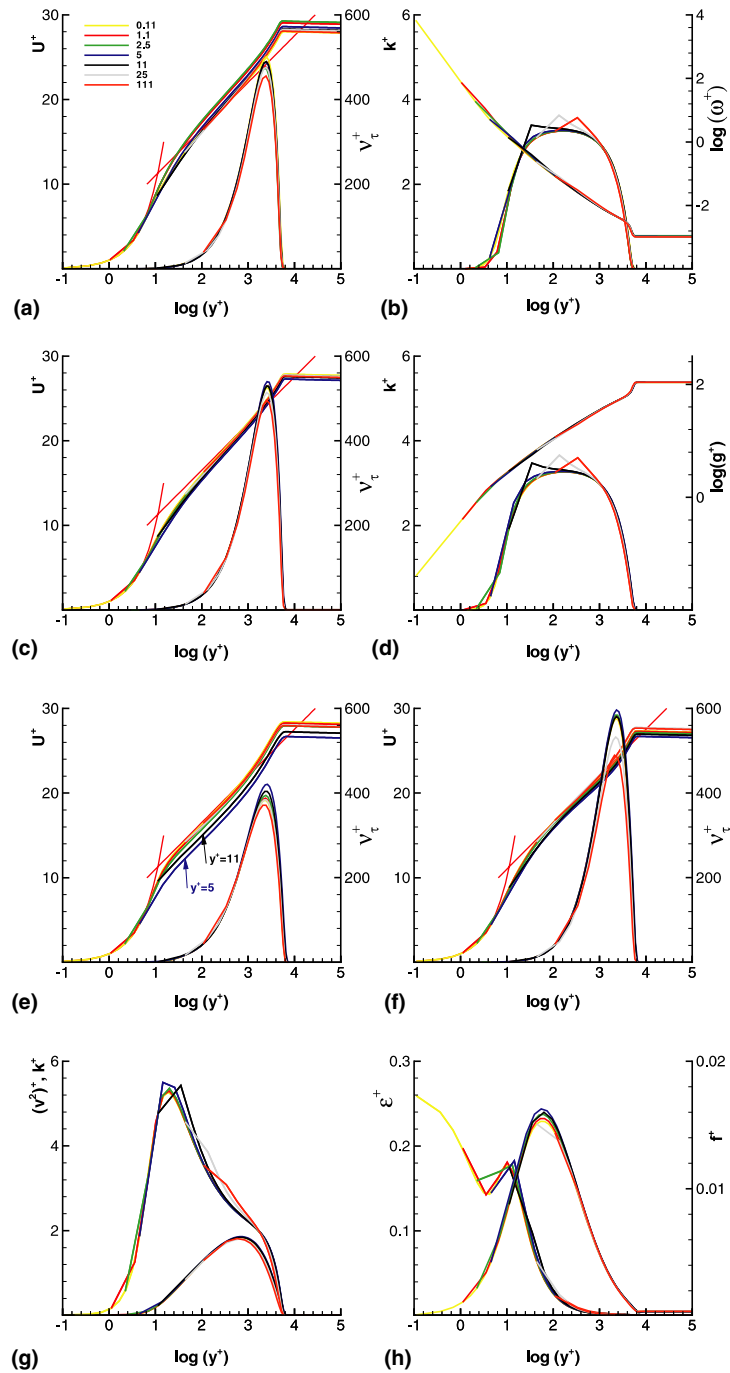Fig. 5. δ-grid: wall integration grid shifted for a distance δ.

Fig. 6. Application of adaptive wall functions using δ-grids. Velocity and eddy-viscosity profiles (a) and k and ω profiles (b), k–ω model; velocity and eddy-viscosity profiles (c) and k and g profiles (d), k–g model; velocity and eddy-viscosity profiles, Spalart–Allmaras (e) and v^2–f model (f); k and v^2 profiles (g) and ε and f profiles (h), v^2–f model.

Fig. 7. Standard application of adaptive wall functions using coarse grids. Velocity and eddy-viscosity profiles (a) and k and ω profiles (b), k–ω model; velocity and eddy-viscosity profiles (c) and k and g profiles (d), k–g model; velocity and eddy-viscosity profiles, Spalart–Allmaras (e), v^2–f model (f); k and v^2 profiles (g) and ε and f profiles (h), v^2–f model.

The spread of the U^+ profiles is very important. In the defect region, this spread will affect the skin friction prediction. The numerical error is dependent on the turbulence model. Among the models that were investigated, the Spalart–Allmaras model is most sensitive to the location of the first cell center. A comparison between k–ω and k–g demonstrates that the change from ω to g reduces the numerical error associated with the near wall behavior of ω. The results also show that, in general, the error is the largest when the first cell center is located in the region $5 < y^+ < 11$, despite the use of correct boundary conditions. The deviation of the eddy-viscosity v_t^+ when the first cell center is at $y^+ = 25$ or $y^+ = 111$ is present for all models. It can be explained by the relative coarseness of the grid throughout the boundary layer as shown in Fig. 5.

4.2. Improving numerical results on coarse grids

An investigation has shown that the numerical error discussed in the previous section is mainly of local character. Increased accuracy of the momentum flux at face 12 has a significant impact on the results.

As shown, the eddy-viscosity is a highly non-linear function of wall distance in the viscous sublayer and the buffer region. The numerical scheme, however, uses a linear interpolation to compute the eddy-viscosity at face 12 (Fig. 8) when computing the diffusive flux. A simple remedy is to enforce the correct value of $v_{t_{12}}^+$ using the corresponding y_{12}^+. This value can be computed from the appropriate analytical expression or look-up table. This can be seen as having a more accurate interpolation scheme at our disposal.

Numerical results obtained with this methodology are presented in Fig. 10. The velocity profiles for Spalart–Allmaras and v^2–f models are significantly improved. It is interesting to note, that even though the diffusive flux has also been improved in the turbulence equations the impact on the turbulence variables is negligible.

In order to demonstrate that the error in the turbulence equations is also of local character a second correction has been investigated. By fixing the correct turbulence variables values in the cell center 2 (e.g. from the look-up tables) the numerical error has been completely eliminated. The results for the turbulence vari-
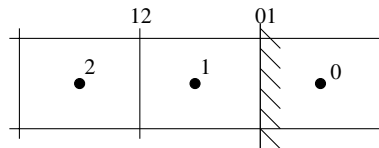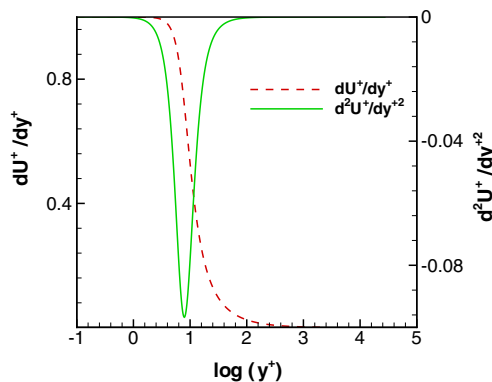

Fig. 8. Near-wall grid structure.

Fig. 9. $\mathrm{d}U^+/\mathrm{d}y^+$ and $\mathrm{d}^2U^+/\mathrm{d}y^{+2}$ computed from Spalding formula.
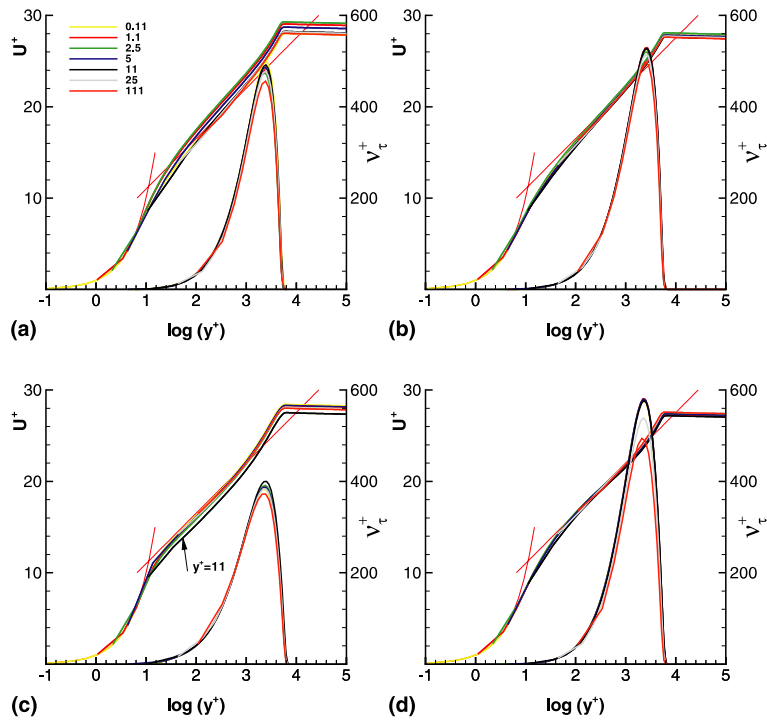
Fig. 10. Adaptive wall functions using coarse grids + imposing $v_{t_{12}}^+$. Velocity and eddy-viscosity profiles, k–ω (a), k–g model (b), Spalart–Allmaras (c), v^2–f model (d).

ables are now nearly perfect as shown in Fig. 12. The velocity profiles are not affected by this modification, except for the k–ω model where a significant improvement is observed as shown in Fig. 11. It is questionable whether this is of much practical value as the use of the look-up table should be limited to the first cell center.
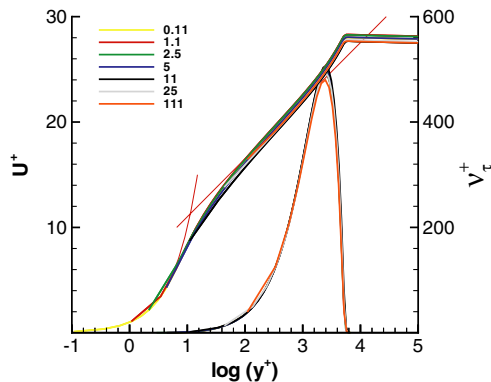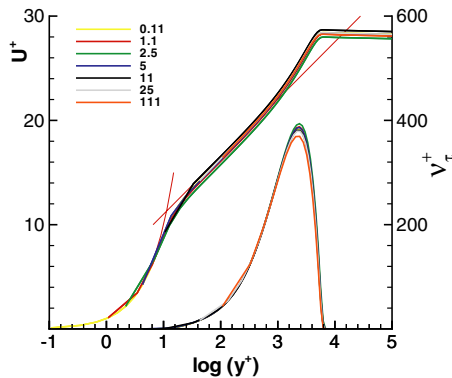

Fig. 11. Velocity and eddy-viscosity profiles for k–ω model; adaptive wall functions using coarse grids + imposing $v_{t_{12}}^+$ and turbulence variables at 2.
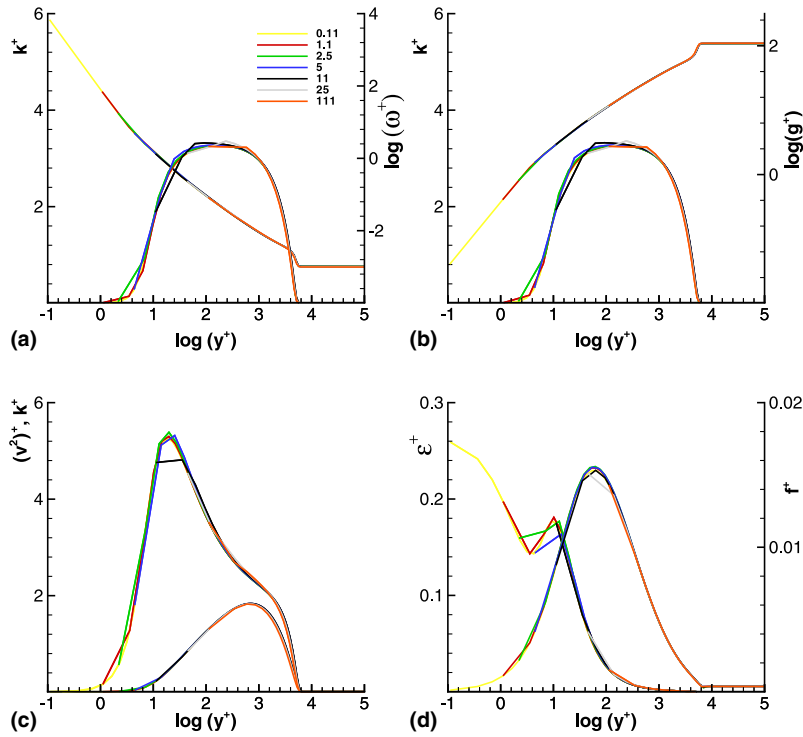
Fig. 12. Adaptive wall functions using coarse grids + imposing $v_{t_{12}}^+$ and turbulence variables at 2. k and g profiles, k–g model (a), k and ω profiles, k–ω model (b) k and v^2 profiles (c) and ε and f profiles (d), v^2–f model.

Curiously, the largest error for the Spalart–Allmaras model in Fig. 10 is for the grid with the first cell center y^+ of 11. A closer look at the velocity profile reveals that the second derivative d^2U^+/dy^{+2} has a spike at approximately that value of y^+, as shown in Fig. 9. In order to investigate the influence of the errors in the velocity gradient computation on the results, we performed an additional simulation for the Spalart–Allmaras model with increased accuracy for the velocity gradient at face 12. This shifts the velocity profile for $y^+ = 11$, as shown in Fig. 13, resulting in a smaller spread of the U^+ profiles.

Fig. 13. Velocity and eddy-viscosity profiles for Spalart–Allmaras model; adaptive wall functions using coarse grids + imposing $v_{t_{12}}^+$ and turbulence variables at 2 with improved accuracy for velocity gradient at 12.

4.3. Recirculating flow

The proposed adaptive wall functions were derived for zero pressure gradient flow over a flat plate. The ability of these wall functions to capture pressure gradient driven separation and reattachment is studied by considering a very simple and reproducible test problem: the boundary layer over a flat plate with an imposed streamwise pressure gradient. The pressure gradient is modulated by suction and blowing applied at a given distance from the plate as illustrated in Fig. 14.

This type of flow was computed with DNS by Na and Moin [11]. We performed RANS computations for that test case and the results are presented in Appendix B. Unfortunately, that case is inappropriate for studying wall functions for several reasons. First, the Reynolds number is very low ($Re_{\theta_{in}} = 300$) and the inflow profile does not have a distinct logarithmic layer therefore reducing the universal region of the boundary layer to $y^+ < 20$. Due to the low Reynolds number the flow is of transitional character. It is well known that RANS turbulence models have significant difficulties predicting transitional flow. This can also be seen from the results in Fig. 24 given in Appendix B. Finally, the suction and blowing jets used in [11] and specified by Eq. (B.1) are positioned adjacent to each other creating a zone of large shear just above the recirculation region. For high Reynolds numbers this shear produces high levels of turbulence which interacts with the recirculation region, a situation that we prefer to avoid.

For the reasons mentioned above, we modified the test case of [11]. We now consider a flat plate of a length L, with $Re_L = 3.6 \times 10^7$ (the flow approaching the recirculation region at $x/L = 0.1$ has a boundary layer with $Re_{\theta_{0.1}} = 6500$). In order to minimize the interaction of the suction and blowing jets as well as the interaction of the blowing jet with the recirculation itself, the vertical velocity component at the upper boundary is prescribed as:

$$v(x) = A\mathrm{e}^{-b(x-x_1)^2} - A\mathrm{e}^{-b(x-x_2)^2}. \tag{41}$$

The parameters in (41) can be adjusted to obtain a desired length and height of the recirculation region. Suction and blowing is specified at a height $h = 1/12\,L$. The vertical velocity is defined with $A = 0.35u_\infty$, $b = 108/L^2$, $x_1 = 0.25L$, $x_2 = 0.75L$. Low levels of freestream turbulence intensity are prescribed at the inflow as well as for the blowing inflow at the upper boundary (see Fig. 14). The computational grid consists of 312×96 cells. A detailed grid-dependence study has shown that this resolution provides sufficient accuracy both in x and y directions.

Streamlines and contours of eddy-viscosity computed using various turbulence models with wall integration are presented in Fig. 15. The skin friction and pressure distribution for zero pressure gradient and for a recirculation-inducing pressure gradient are reported in Fig. 16. The results show significant sensitivity of the solution to the model. The length of the recirculation region scaled with the displacement thickness $\delta_{0.1}^*$
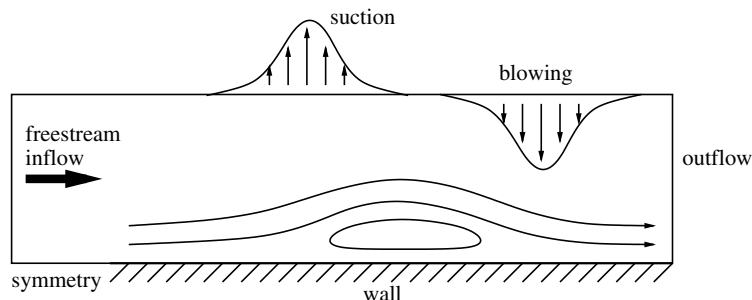

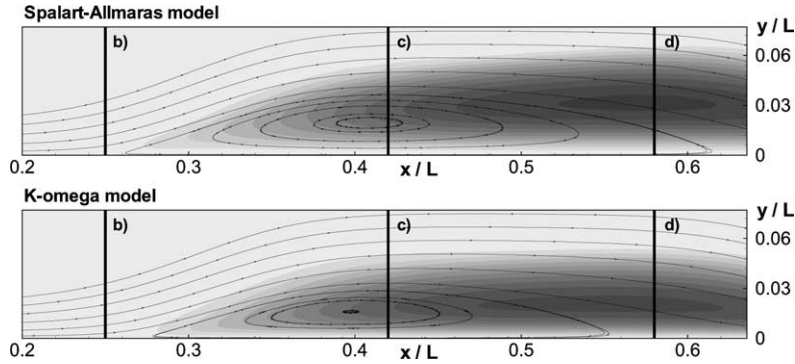Fig. 14. Flat plate with separation induced via suction and blowing at the upper boundary.

Fig. 15. Streamlines showing the recirculation and contours of eddy-viscosity. The location of three of the velocity profiles presented in Figs. 22 and 23 is indicated by (b–d).

at $x/L = 0.1$ is in the range of $1000 < L_{\text{rec}}/\delta^*_{0.1} < 1600$. Thus by modifying the suction and blowing profile and the Reynolds number the recirculation region is here significantly larger than the one presented in Appendix B.

In order to assess the performance of the proposed adaptive wall functions (used here without numerical corrections discussed in Section 4.2), we consider grids with the first cell center at $y^+ = 0.11$, 1.1, 2.5, 5, 11, 25, 111, at the entrance. Note that in contrast to the flat plate the y^+ values vary considerably in the recirculation region. Fig. 17 shows the variation of first cell center y^+ along the plate. In the recirculation region, the y^+ values are significantly smaller than the corresponding flat plate y^+ values.

Numerical indicate that the proposed wall functions function properly for Spalart–Allmaras and k–ω models (the same behavior was observed for k–g model). The skin friction coefficients computed using wall integration and wall functions on the $y^+ = 0.11$ grid coincide. In contrast, the skin friction computed with the v^2–f model using wall functions differ slightly from the wall integration solution on the $y^+ = 0.11$ grid as shown in Fig. 20(a). This might be caused by the non-zero boundary condition for ε^+ and its scaling with u_τ. As shown in Fig. 20(b), ε^+ is singular near the separation and reattachment points where u_τ approaches zero. In the current wall function concept, however, ε^+ in the first cell center is set to a constant value of ≈ 0.26. This problem may be alleviated by using a more appropriate scaling for ε^+.
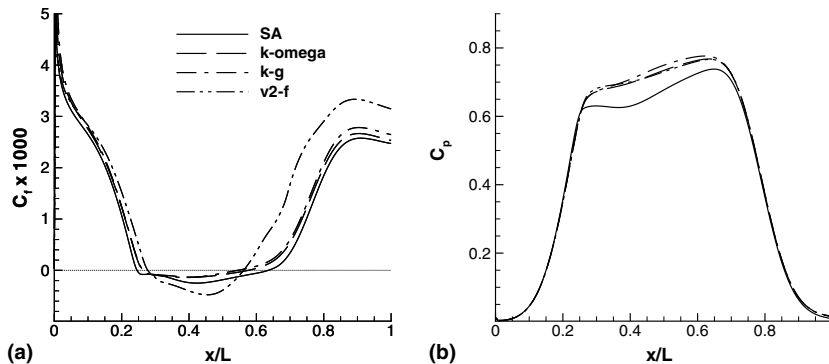

Fig. 16. Skin friction (a) and pressure distribution (b) for the flow with recirculation with v^2–f, k–ω, k–g and Spalart–Allmaras models.
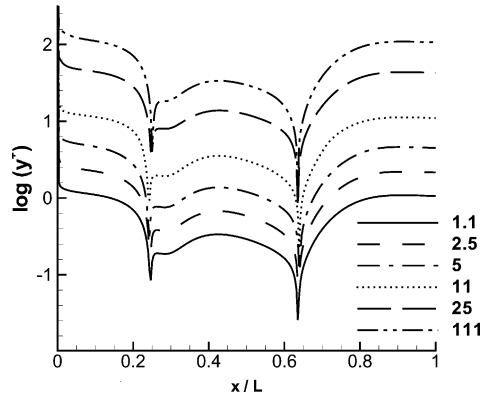
Fig. 17. First cell center y^+ values for the flow with recirculation with Spalart–Allmaras model using wall functions.
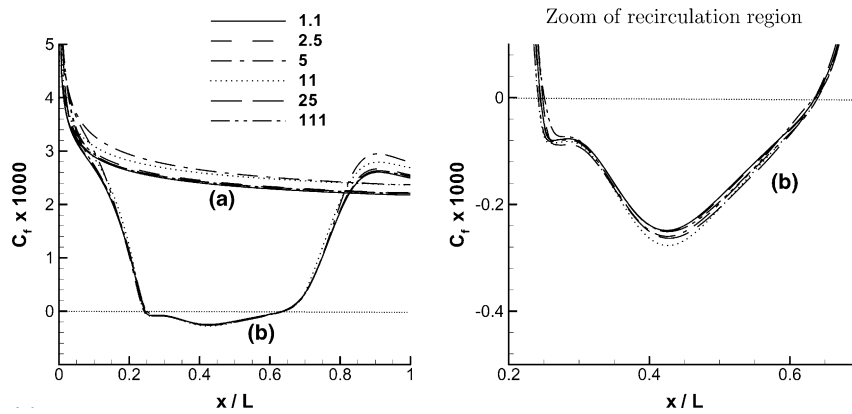

Fig. 18. Skin friction for zero pressure gradient (a) and adverse/favorable pressure gradient (b) using Spalart–Allmaras model: comparison of wall-functions results.
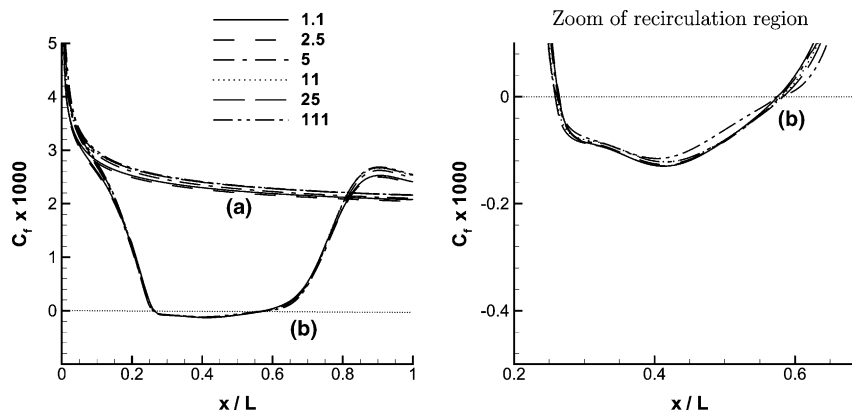

Fig. 19. Skin friction for zero pressure gradient (a) and adverse/favorable pressure gradient (b) using k–ω model: comparison of wall-functions results.

Detailed coarse grid results are presented for Spalart–Allmaras and k–ω models. Surprisingly, numerical results presented in Figs. 18 and 19 show that skin friction in the recirculation region is not sensitive to the first cell center y^+ value. Despite the fact that pressure gradient and convection effects are not included in the wall-function formulation the wall functions remain usable in that region. That may be because the solution near the wall in the recirculation region scales similarly to the flat plate. Indeed, it is shown in Figs. 22 and 23 that, up to a certain y^+, non-dimensional velocity and turbulent kinetic energy profiles collapse onto the look-up table profiles which were computed for zero pressure gradient flow over a flat plate. The universal region extends over a larger range of y^+ values for Spalart–Allmaras than for the k–ω model. Turbulent kinetic energy profiles for the k–ω model show a smaller extent of the universal region. This may explain why the velocity profiles for the k–ω model start to deviate earlier from the universal solution.

Coincidentally, the coarsest grid used in this analysis (see circles in Figs. 22 and 23) is still able to represent the recirculation region accurately. Obviously, this is influenced by the size of the recirculation. A smaller recirculation region may not be sufficiently resolved with such a coarse grid and the first cell center may lie outside the universal region.

For completeness, v^2–f results are also included. Despite the observed inconsistency described above, the wall functions are still able to predict the recirculation region as shown in Fig. 21. However, the sensitivity to the first cell center y^+ value is significant.
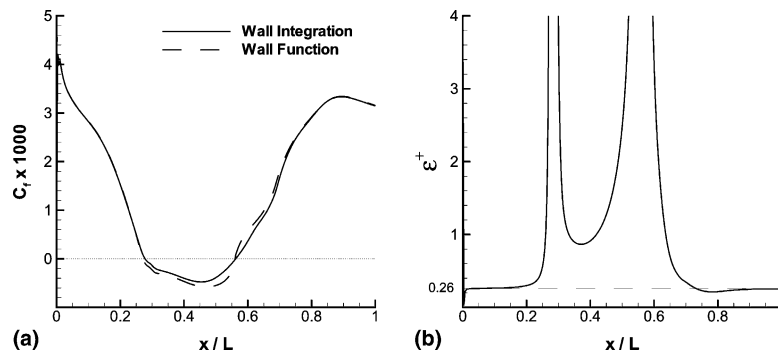
Fig. 20. (a) Comparison of skin friction computed with the v^2–f model for $y^+ = 0.11$ grid using wall integration and wall functions; (b) Distribution of ε^+ in the first cell center computed using wall integration.
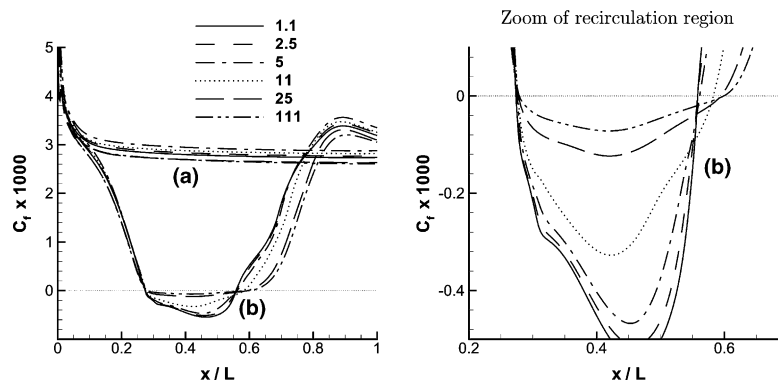
Fig. 21. Skin friction for zero pressure gradient (a) and adverse/favorable pressure gradient (b) using v^2–f model: comparison of wall-functions results.
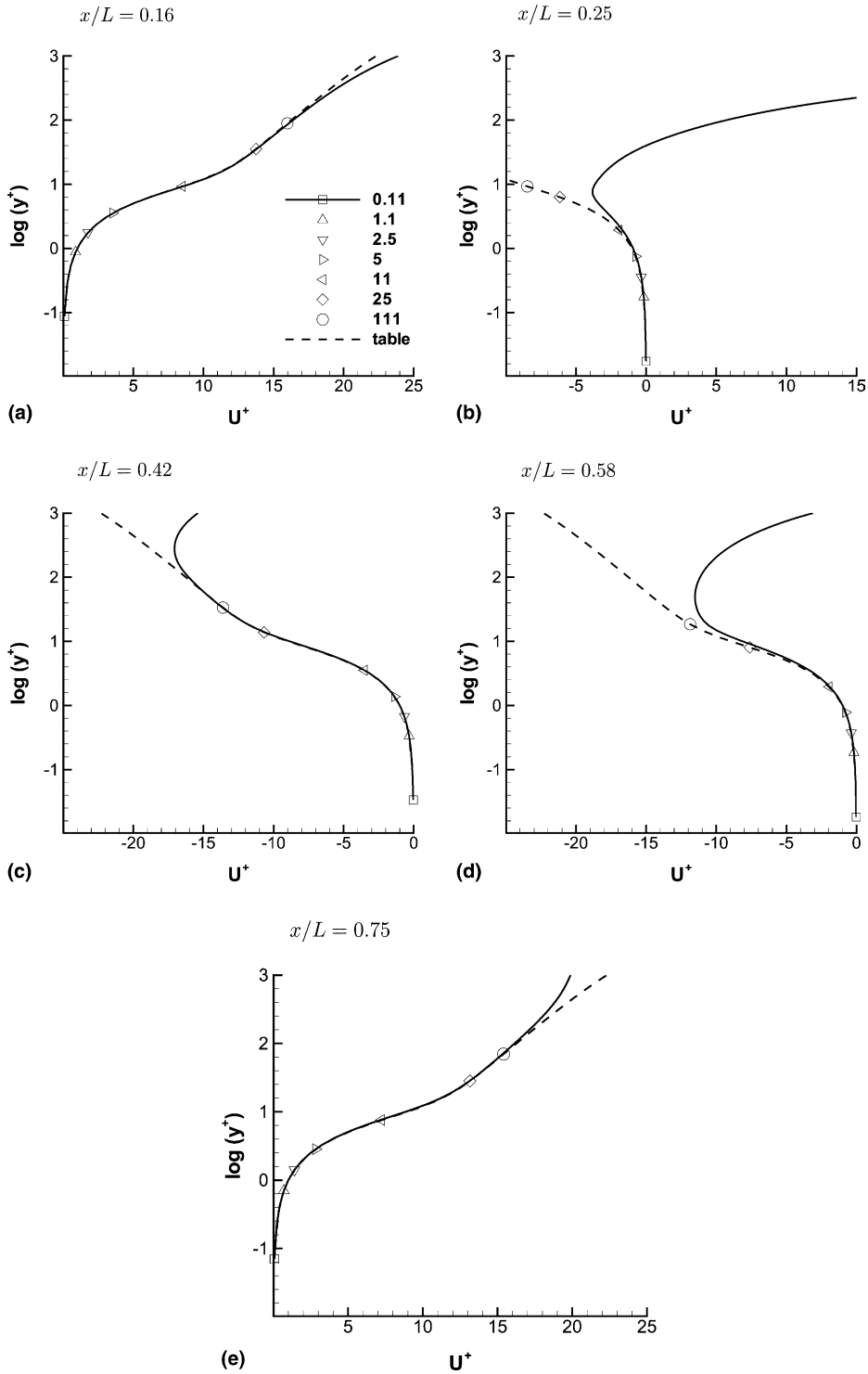
Fig. 22. Velocity profiles for the flow with recirculation (Spalart–Allmaras model).
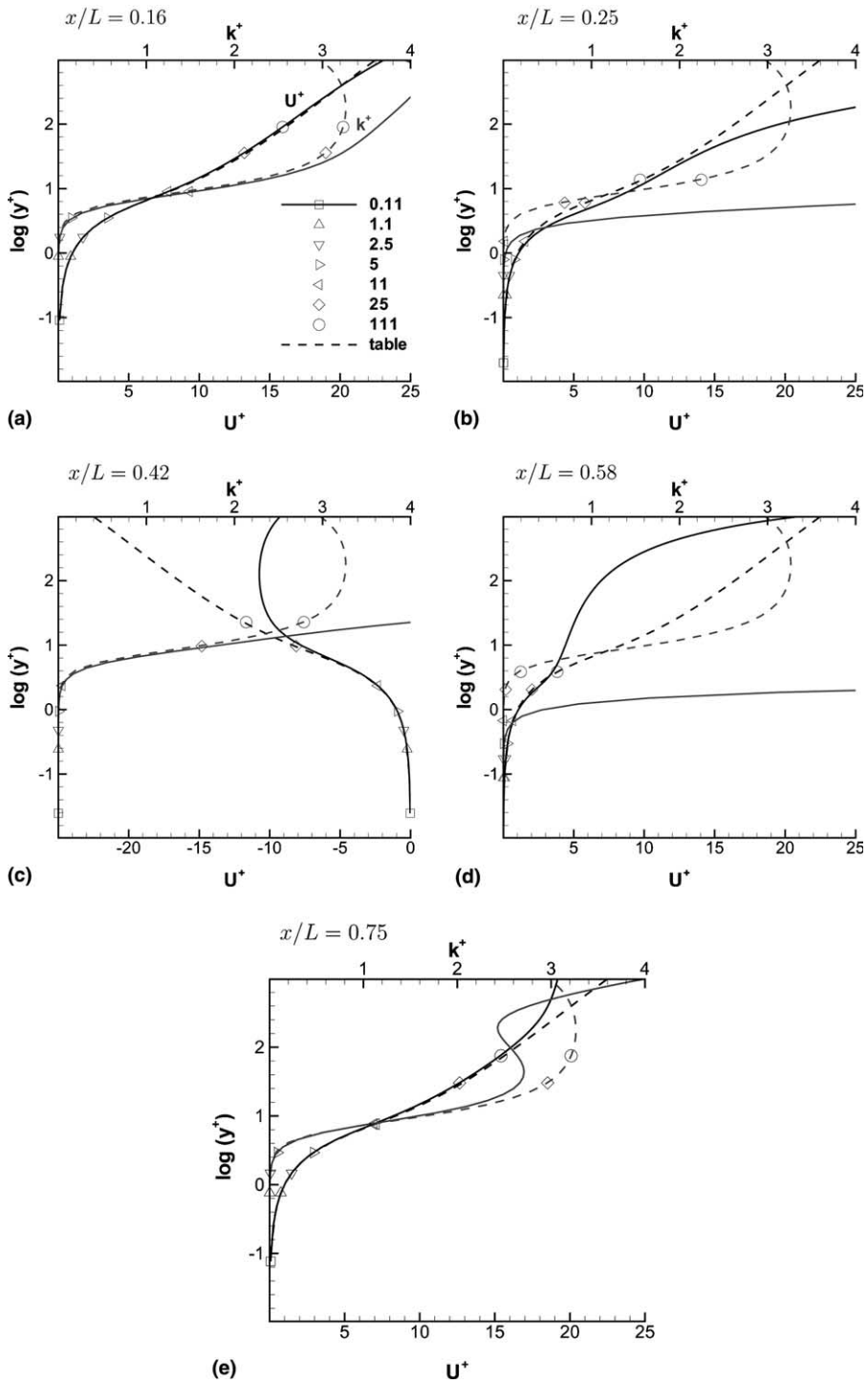
Fig. 23. Velocity and k profiles for the flow with recirculation (k–ω model).

5. Conclusions

This paper discusses the near wall behavior of various advanced RANS turbulence models focusing on the viscous sublayer and logarithmic layer. The analysis has implications for adaptive wall functions to be used on grids that have a significantly lower resolution of the boundary layer than the typical wall integration grids.

New analytical solutions for the v^2–f model have been derived for the viscous sublayer and the logarithmic layer. These provide an insight into the physics of the model. For the Spalart–Allmaras model, a simple wall function has been proposed that is based entirely on the near wall analytical solution.

The analysis of the existing wall functions for the k–ω model has shown significant deficiencies. These are overcome by the adaptive wall function approach that we are proposing. It is also shown, that a simple variable transformation, from ω to g, circumvents the well known difficulties with ω in the viscous sublayer.

In general, there is no satisfactory analytical approximation for the intermediate region (excluding Spalart–Allmaras model). The look-up table concept seems to be an accurate and practical approach. Indeed, the obtained numerical results are very satisfactory.

The look-up table concept allows an explicit evaluation of the friction velocity u_τ which is usually obtained with an iterative method. The tables may also be used to improve numerical stability. It is well known that the v^2–f model defined with $N = 1$ requires a coupled numerical solution of the model equations due to the stiffness of the f boundary condition. The use of wall functions substitutes this boundary condition removing the stiffness caused by it.

The proposed test case for the recirculating flow is very attractive since it eliminates the uncertainty related to the effects of curvature and quality of computational grid usually associated with recirculating flows. The numerical results show that proposed wall function concept is applicable and accurate when the grid resolution is sufficient for the given size of the recirculation region.

The adaptive wall functions are being tested for complex applications. Depending on the success with these computations, future work on wall functions may focus on modifications considering pressure gradient and convection effects.

Finally, the look-up table concept may also be easily adapted to more complicated turbulence models such as Reynolds Stress Models.

Appendix A. RANS equations

This section contains the governing flow and turbulence models equations. The continuity equation is

$$\nabla \cdot u = 0. \tag{A.1}$$

The momentum equations are:

$$\partial_t u_i + u \cdot \nabla u_i = -\frac{1}{\rho}\nabla_i p + \nabla \cdot [(v + v_t)\nabla u_i]. \tag{A.2}$$

A.1. Spalart–Allmaras turbulence model

The Spalart–Allmaras model [13] consists of one transport equation

$$\partial_t \tilde{v} + u \cdot \nabla \tilde{v} = Q(\tilde{v}) + \frac{c_{b2}}{c_{b3}} \nabla \tilde{v} \cdot \nabla \tilde{v} + \frac{1}{c_{b3}} \nabla \cdot [(v + \tilde{v}) \nabla \tilde{v}], \tag{A.3}$$

where the source term $Q(\tilde{v})$ is

$$Q(\tilde{v}) = c_{b1}(1 - f_{t2}) \tilde{S} \tilde{v} + \left(\frac{c_{b1}}{\kappa^2} f_{t2} - c_{w1} f_w\right) \left(\frac{\tilde{v}}{d}\right)^2. \tag{A.4}$$

The eddy-viscosity is

$$v_t = \tilde{v} f_{v1}. \tag{A.5}$$

The model damping functions, auxiliary relations and the trip term are defined as

$$f_{v1} = \frac{\chi^3}{\chi^3 + c_{v1}^3}, \quad f_{v2} = 1 - \frac{\chi}{1 + \chi f_{v1}}, \quad \chi = \frac{\tilde{v}}{v}, \tag{A.6}$$

$$f_w = g \left[\frac{1 + c_{w3}^6}{g^6 + c_{w3}^6}\right]^{\frac{1}{6}}, \quad g = r + c_{w2}(r^6 - r), \quad r = \frac{\tilde{v}}{\tilde{S}\kappa^2 d^2}, \tag{A.7}$$

$$\tilde{S} = S + \frac{\tilde{v}}{\kappa^2 d^2} f_{v2}, \quad S = \sqrt{2 S_{ij} S_{ij}}, \quad f_{t2} = c_{t3} \exp(-c_{t4} \chi^2). \tag{A.8}$$

The variable d is the distance to the nearest wall, κ the von Kármán constant and the strain rate tensor is $S_{ij} = \frac{1}{2}(\partial_j u_i + \partial_i u_j)$. Finally, the model closure coefficients are

$$c_{b1} = 0.1355, \quad c_{b2} = 0.622, \quad c_{b3} = 2/3, \quad c_{v1} = 7.1, \tag{A.9}$$

$$c_{w1} = \frac{c_{b1}}{\kappa^2} + \frac{1 + c_{b2}}{c_{b3}}, \quad c_{w2} = 0.3, \quad c_{w3} = 2, \quad c_{t3} = 1.2, \quad c_{t4} = 0.5. \tag{A.10}$$

The wall boundary condition is

$$\tilde{v} = 0. \tag{A.11}$$

A.2. k–ω model

In the Wilcox's original, k–ω model [17], the eddy-viscosity is defined as:

$$v_t = k/\omega. \tag{A.12}$$

The equation for turbulent kinetic energy is

$$\partial_t k + u \cdot \nabla k = P_k - C_\mu \omega k + \nabla \cdot [(v + \sigma_k v_t) \nabla k], \tag{A.13}$$

where

$$P_k = v_t S^2, \quad S = \sqrt{2 S_{ij} S_{ij}}. \tag{A.14}$$

The equation for the specific dissipation rate ω is

$$\partial_t \omega + u \cdot \nabla \omega = \frac{\gamma_1 \omega}{k} P_k - \beta_1 \omega^2 + \nabla \cdot [(v + \sigma_\omega v_t) \nabla \omega]. \tag{A.15}$$

The original model constants are

$$\sigma_k = \sigma_\omega = 0.5; \quad \gamma_1 = 5/9; \quad \beta_1 = 0.075; \quad C_\mu = 0.09.$$

The wall boundary condition for k is:

$$k = 0. \tag{A.16}$$

At the wall, the specific dissipation rate ω asymptotically tends to infinity as $\sim 1/y^2$. In [10], it was suggested to use the following boundary condition

$$\omega = \frac{60v}{\beta_1 d_1^2}, \tag{A.17}$$

where d_1 is the distance from the wall to the cell center of the first cell above the wall.

A.3. k–g model

The equations of the k–g model [6] are:

$$\partial_t k + u \cdot \nabla k = P_k - \frac{k}{g^2} + \nabla \cdot [(v + \sigma_k v_t)\nabla k] \tag{A.18}$$

$$\partial_t g + u \cdot \nabla g = -\alpha \frac{g}{2} P_k + \frac{\beta_1}{2g C_\mu} - (v + \sigma_g v_t)\frac{3}{g}\nabla g \cdot \nabla g + \nabla \cdot [(v + \sigma_g v_t)\nabla g], \tag{A.19}$$

with the eddy-viscosity defined as

$$v_t = C_\mu k g^2. \tag{A.20}$$

The wall boundary conditions for the k–g model are

$$k = 0, \quad g = 0. \tag{A.21}$$

A.4. v^2–f model

In [4], the eddy-viscosity is defined as

$$v_t = C_\mu \overline{v^2} T \tag{A.22}$$

with the turbulence timescale

$$T = \min\left[\max\left[\frac{k}{\varepsilon}, 6\sqrt{\frac{v}{\varepsilon}}\right], \frac{\alpha k}{\sqrt{3\overline{v^2}} C_\mu S}\right] \tag{A.23}$$

with $\alpha = 0.6$.

The equation for turbulent kinetic energy is

$$\partial_t k + u \cdot \nabla k = P_k - \varepsilon + \nabla \cdot [(v + v_t)\nabla k], \tag{A.24}$$

where P_k is defined as in (A.14). Eq. (A.24) is supplemented by

$$\partial_t \varepsilon + u \cdot \nabla \varepsilon = \frac{C_{\varepsilon 1} P_k - C_{\varepsilon 2}\varepsilon}{T} + \nabla \cdot \left[\left(v + \frac{v_t}{\sigma_\varepsilon}\right)\nabla \varepsilon\right]. \tag{A.25}$$

In addition to the equations for k and ε, the model includes an equation for $\overline{v^2}$

$$\partial_t \overline{v^2} + u \cdot \nabla \overline{v^2} = kf - N\frac{\overline{v^2}}{k}\varepsilon + \nabla \cdot [(v + v_t)\nabla\overline{v^2}] \tag{A.26}$$

with f representing the non-local effects:

$$f - L^2 \Delta f = (C_{f1} - 1)\frac{2/3 - \overline{v^2}/k}{T} + C_{f2}\frac{P_k}{k} + (N-1)\frac{\overline{v^2}}{kT}, \tag{A.27}$$

where the turbulent length scale L is

$$L = C_L \max\left[\min\left[\frac{k^{3/2}}{\varepsilon}, \frac{k^{3/2}}{\sqrt{3\overline{v^2}}C_\mu S}\right], C_\eta\frac{v^{3/4}}{\varepsilon^{1/4}}\right]. \tag{A.28}$$

For solid walls, when $d \to 0$, this yields:

$$k(0) = 0, \qquad \overline{v^2}(0) = 0, \quad \varepsilon \to \frac{2vk}{d^2}, \quad f \to -\frac{4(6-N)v^2\overline{v^2}}{\varepsilon d^4}. \tag{A.29}$$

The original v^2–f model with $N = 1$ was later modified (see [1,9]) in order to avoid the numerical difficulties due to strong nonlinear coupling of turbulence variables through the boundary conditions (A.29). The value $N = 6$ results in $f = 0$ at viscous walls. In addition, the wall distance d has been eliminated from the equation for $C_{\varepsilon1}$. The model constants are:

$$C_\mu = 0.22; \quad C_{\varepsilon1} = 1.4(1 + 0.050\sqrt{k/\overline{v^2}}); \quad C_{\varepsilon2} = 1.9;$$

$$C_{f1} = 1.4; \quad C_{f2} = 0.3; \quad C_L = 0.23; \quad C_\eta = 70. \tag{A.30}$$

Appendix B. Comparison with DNS for recirculating flow

The direct numerical simulation (DNS) of recirculating flow by Na and Moin [11] is analyzed to assess the performance of RANS turbulence models. The DNS test case consists of a boundary layer over a flat plate with an imposed pressure gradient modulated by suction and blowing at a given distance from the plate. In contrast to the test case shown in Fig. 14, an inflow profile is applied at the beginning of the plate. The inflow profile is obtained from Spalart's DNS [14] for Reynolds number $Re_\theta = 300$. The dimensions of the computational domain are: $350\delta_{in}^* \times 64\delta_{in}^*$, where δ_{in}^* is the displacement thickness for the inflow profile. The vertical velocity component at the upper boundary is:

$$v(x) = A(x_0 - x)e^{-b(x_0-x)^2}, \tag{B.1}$$

with $A = 0.019u_\infty/\delta_{in}^*, b = 2.31 10^{-4}/\delta_{in}^{*\,2}$ and $x_0 = 221.4\delta_{in}^*$.

For the RANS computations, the inflow profiles for various variables were computed from Spalart's DNS data. The turbulent kinetic energy is computed from the turbulence intensities $k = (u_{rms}^2 + v_{rms}^2 + w_{rms}^2)/2$, the variable $\overline{v^2}$ is set to v_{rms}^2 and the eddy-viscosity is computed from the Reynolds stress $v_t = -\langle uv\rangle/(dU/dy)$. The variables ω and g follow directly from the eddy-viscosity definitions (A.12) and (A.20), respectively. The dissipation rate ϵ and the modified viscosity $\tilde{v}$ are obtained iteratively from Eqs. (A.22) and (A.5), respectively. df/dn is set to zero.

Skin friction and pressure coefficients computed using various turbulence models are compared with DNS data in Fig. 24. The results for skin friction show that all four turbulence models predict separation and that the reattachment location agrees well with the DNS. However, the location of the separation point
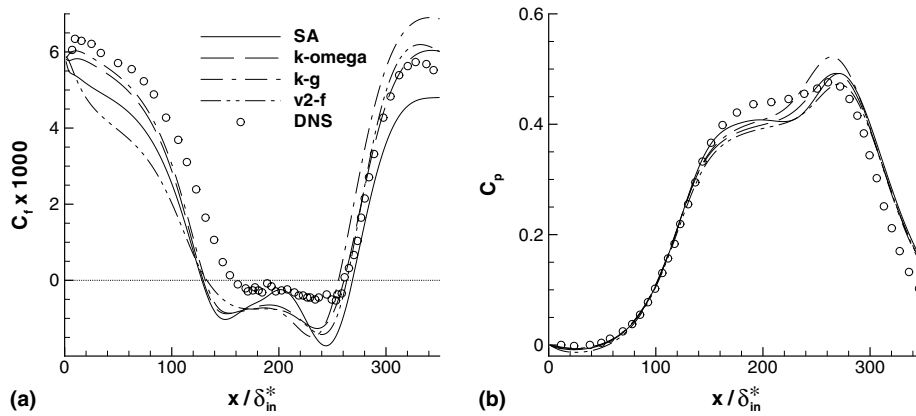
Fig. 24. Skin friction (a) and pressure coefficient (b) for recirculating flow at $Re_{\theta,inflow} = 300$.

is predicted too early and the skin friction is underpredicted upstream of the recirculation region. That can be explained by the transitional nature of the inflow at $Re_\theta = 300$. Spalart discusses this in detail in [14]. The Reynolds stress $-\langle uv \rangle^+$ does not approach unity in the logarithmic layer, indeed it decreases with $y^+ > 30$ (see Fig. 9 in [14]). It is well known that RANS models differ significantly in the prediction of transitional flows. For this flow, k–ω and k–g transition to turbulence earlier while Spalart–Allmaras and v^2–f retain a laminar character longer.

References

[1] M. Behnia, S. Parneix, Y. Shabany, P.A. Durbin, Numerical study of turbulent heat transfer in confined and unconfined impinging jets, Int. J. Heat Fluid Flow 20 (1999) 1–9.
[2] D.B. DeGraaff, J.K. Eaton, Reynolds number scaling of the flat plate turbulent boundary layer, JFM 422 (2000) 319–386.
[3] P.A. Durbin, B.A. Pettersson Reif, Statistical Theory and Modeling for Turbulent Flow, Wiley, 2001.
[4] P.A. Durbin, Separated flow computations with the k–ϵ–$\overline{v^2}$ model, AIAA J. 33 (1995) 659–664.
[5] Holmes G., Mitchell B., 2003. Private communication.
[6] G. Kalitzin, Validation and development of two-equation turbulence models, in: W. Haase, et al. (Eds.), Validation of CFD Codes and Assessment of Turbulence Models, Notes on Numerical Fluid Mechanics Series, 57, Vieweg, 1997.
[7] G. Kalitzin, G. Iaccarino, Toward immersed boundary simulation of high Reynolds number flows, CTR Ann. Res. Briefs (2003) 369–378.
[8] B.E. Launder, D.B. Spalding, The numerical computation of turbulent flows, Comp. Meth. Appl. Mech. Eng. 3 (3) (1974) 269–289.
[9] F.S. Lien, G. Kalitzin, Computations of transonic flows with the v^2–f turbulence model, Int. J. Heat Fluid Flow 22 (2001) 53–61.
[10] F.R. Menter, Zonal two-equation k–ω turbulence model predictions. AIAA Paper No. 93-2906, 1993.
[11] Y. Na, P. Moin, 1996. Direct numerical simulation of turbulent boundary layers with adverse pressure gradient and separation. Ph.D. thesis, Mech. Eng. Dept., Stanford University.
[12] H. Schlichting, Boundary Layer Theory, seventh ed., McGraw-Hill, 1979.
[13] P.R. Spalart, S.R. Allmaras, A one-equation turbulence model for aerodynamic flows, La Rech. Aerospatiale 1 (1994) 1–23.
[14] P.R. Spalart, Direct simulation of a turbulent boundary layer up to $R_\Theta = 1410$, JFM 187 (1988) 61–98.
[15] D.B. Spalding, A single formula for the law of the wall, Trans. ASME., J. Appl. Mech. 28 (1961) 444–458.
[16] W. Vieser, T. Esch, F.R. Menter, 2002. Heat transfer predictions using advanced two-equation turbulence models. CFX Technical Memorandum CFX-VAL10/0602.
[17] D.C. Wilcox, Turbulence Modeling for CFD, DCW Industries, Inc., La Canada, CA, 1993.
[18] CITS 2003. Annual Technical Report, Center for Integrated Turbulence Simulations, Stanford University.
[19] CFX 2003. Version 5.6, User Manual: Turbulence and Wall Function Theory.
[20] Fluent 2003. Version 6.1, User Manual.
[21] StarCD 2001. Version 3.15 Methodology, Computational Dynamics Limited.